energies

MDPI

Article

Optimized Feedback Type Flux Weakening Control of Non-Salient Permanent Magnet Synchronous Machines in MTPV Region with Improved Stability

Chao Wang, Ziqiang Zhu *, Lei Xu, Ximeng Wu and Kejin Lu

School of Electronic and Electrical Engineering, University of Sheffield, Mappin Street, Sheffield S1 3JD, UK; cwang1276@163.com (C.W.); 15802185302@163.com (L.X.); wxmstronger@gmail.com (X.W.); klu12@sheffield.ac.uk (K.L.)
* Correspondence: z.q.zhu@sheffield.ac.uk

Abstract: This paper introduces an enhanced approach for optimizing the flux-weakening performance of a non-salient permanent magnet synchronous machine (PMSM), by incorporating the maximum torque per voltage (MTPV) region into a conventional voltage magnitude feedback control strategy. The MTPV control strategy is initially optimized for steady-state performance by incorporating the effect of resistance, which plays a crucial role in small power motors. To maintain stability and good dynamics in the flux-weakening region, a current command feedback MTPV controller is utilized, as opposed to a voltage command feedback approach. Additionally, to address stability concerns in the MTPV region, a feedback type proportional-integral (PI) MTPV controller is designed and implemented. The stability in both the over-modulation and various flux-weakening regions is further enhanced using a voltage vector modifier (VVM). Therefore, the proposed feedback-based flux-weakening control enhances system steady-state performance, dynamic response, and stability across both linear and over modulation regions under various flux-weakening conditions, making it suitable for general-purpose applications. The effectiveness of the proposed method is validated through experimental results.

Keywords: current command feedback; flux-weakening control; MTPV; non-salient PMSM; resistance; stability; over modulation

Academic Editor: Daniel Morinigo-Sotelo

Received: 21 March 2025
Revised: 14 April 2025
Accepted: 26 April 2025
Published: 29 April 2025

Citation: Wang, C.; Zhu, Z.; Xu, L.; Wu, X.; Lu, K. Optimized Feedback Type Flux Weakening Control of Non-Salient Permanent Magnet Synchronous Machines in MTPV Region with Improved Stability. *Energies* **2025**, *18*, 2282. https://doi.org/10.3390/en18092282

1. Introduction

Permanent magnet synchronous machine (PMSM) is widely used in applications such as electric vehicles, aerospace, and industrial automation due to its high efficiency and high torque/power density [1]. To extend the speed operation range under the physical limit of the machine and inverter, the flux-weakening methods are normally employed [2].

Within the conventional current vector control framework, flux-weakening methods have been developed to optimize current commands under current and voltage constraints [3]. The current commands can be obtained by the feedforward [4,5], voltage feedback [6,7], and hybrid methods [8,9]. While the feedforward method offers excellent transient performance [10], its effectiveness is significantly affected by variations in machine parameters. For the small power machine, the complexity of the optimal d- and q-axis current equations increases significantly when the resistance is considered [11]. In [11], a piecewise linearization method is employed to realize a simplified current trajectory, making it suitable for low-cost applications. Nevertheless, this approach is unable to generate the optimal current trajectory in the flux-weakening region.

By introducing a voltage feedback loop, the voltage feedback method enables automatic flux-weakening control [12]. It can achieve an optimal current trajectory and have robustness against variation of the machine parameters [13]. The implementation of the feedback method is much simpler than the hybrid method which requires both feedback and feedforward paths. Owing to its simplicity, the voltage feedback method has been widely adopted in both low-cost applications and industrial practices [14]. However, the feedback controller requires the proper tuning of control parameters. In [15] and [16], an adaptive control parameter method is employed to enable a stable and extended flux-weakening operation range. However, its application is restricted to the linear modulation region (LMR). While the LMR offers improved dynamics and reduced current harmonics, it comes at the cost of reduced DC-link voltage utilization.

In the flux-weakening and over-modulation regions, a reduction in the voltage control margin may lead to conflicts between the dq-axis current controllers, potentially resulting in oscillations and instability [17]. Reference [17] proposes using a single d-axis current controller, while leaving the q-axis voltage in an open-loop configuration, effectively resolving the conflict between the d- and q-axis current controllers. However, the q-axis voltage reference relies on the machine parameters, which cannot guarantee the optimal current trajectory and may have larger current ripple due to its partial open-loop structure. In [18–20], different control structures are employed depending on the operating region of the machine. In the constant torque region, the conventional dual current closed-loop structure is maintained. In the flux-weakening region, the control strategy regulates the voltage angle while keeping the voltage magnitude constant. As a result, the conflict between current regulators is eliminated in the flux-weakening region, allowing for better voltage utilization. However, an additional transition criterion between the constant torque and flux-weakening regions is required, which is determined through trial and error [20]. Reference [21] demonstrates the achievement of instantaneous current control in the flux-weakening region, even under six-step mode, by incorporating a straightforward voltage vector modifier (VVM). This approach enhances stability and current dynamics in the over-modulation region while maintaining dual-current control structure.

In machines with high inductance [22–25] or under overload conditions, the characteristic current may fall below the current limit. Under such condition, the MTPV control is required to maximize the torque capability and achieve infinite constant power speed ratio (CPSR) [26]. In [23], the demagnetizing d-axis current command is generated by utilizing the voltage difference between the input and output of the over modulation block, the MTPV control on a non-salient PMSM is achieved by forcing the MTPV penalty function to zero with an extra voltage feedback loop. Although the voltage difference feedback controller can achieve a quasi six-step operation, it cannot achieve flux-weakening operation in LMR. In order to achieve flux-weakening in both linear and over modulation regions while maintain the dual current control structure, the conventional voltage magnitude feedback controller has to be employed [21]. However, the MTPV region is not considered in [21]. In this paper, feedback MTPV control is proposed based on the conventional voltage magnitude feedback controller. In addition, the MTPV controller is optimized in terms of steady-state performance, dynamic performance, and the stability. Initially, the MTPV penalty function is refined by accounting for the resistance effect, which is crucial for small power machines. Subsequently, a current command feedback MTPV controller is implemented, instead of the voltage command feedback MTPV controller used in [23] and [9], to maintain stability while ensuring robust dynamic performance. Additionally, to address stability concerns in the MTPV region, the MTPV loop is thoroughly analyzed, and a feedback type PI MTPV controller is designed, a method not commonly explored in other studies. Furthermore, stability in the over-modulation region is enhanced through the use of a VVM, building upon the approach outlined in [21]. The proposed strategy enhances steady-state performance, dynamic response, and stability in both the linear and over-modulation regions, across various flux-weakening conditions.

This paper extends the work in [14] with extensive experimental results and is organized as follows: Section 2 provides an overview of the operational regions and control strategies for machines with an MTPV region. In Section 3, the feedback-based MTPV control strategy is refined, including the optimization of its penalty function and controller design. The performance in the over-modulation region is enhanced through the use of a VVM. Section 4 presents the experimental validation, followed by the conclusions in Section 5.

2. Feedback Type Control Strategies

2.1. Machine Model

The mathematical model of non-salient PMSM in the synchronous dq reference frame can be expressed as

$$\begin{cases} V_d = R_s i_d + L_s \frac{di_d}{dt} - \omega_e L_s i_q \\ V_q = R_s i_q + L_s \frac{di_q}{dt} + \omega_e (L_s i_d + \psi_m) \\ \frac{J}{N_P} \frac{d\omega_e}{dt} = T_e - T_L \\ T_e = 1.5 N_P \psi_m i_q \end{cases} \tag{1}$$

where V, i are the stator voltage and current, respectively; the subscripts d and q indicate the relevant components in d- and q-axes; R_s is the stator resistance; L_s is the synchronous inductance; ω_e is the electrical angular speed; ψ_m is the permanent magnet flux linkage; T_l is the load torque; J is the moment of inertia; N_p is the number of pole pairs.

2.2. Operating Regions

There are two supply constraints, i.e., current and voltage limits, which can be written as

$$\begin{cases} |\boldsymbol{I}_s|^2 = i_d^2 + i_q^2 \leq I_m^2 \\ |\boldsymbol{V}_s|^2 = V_d^2 + V_q^2 \leq V_m^2 \end{cases} \tag{2}$$

where $\boldsymbol{I}_s$ and $\boldsymbol{V}_s$ are the current and voltage vectors, in dq reference frame, they are $(i_d + ji_q)$ and $(V_d + jV_q)$, respectively; I_m is the current limit, which is mainly restricted by the thermal limit of machine and inverter; V_m is the voltage magnitude limit which is mainly restricted by the DC-link voltage V_{dc}.

At steady state, the inductive voltage drop on inductance can be ignored. In addition, by also considering the resistance of the power switch device and power cable, the voltage constraint described in the d- and q-axis current plane can be derived as

$$(i_d + \frac{\omega_e^2 L_s \psi_m}{Z_s^2})^2 + (i_q + \frac{\omega_e R \psi_m}{Z_s^2})^2 = \frac{V_m^2}{Z_s^2} \tag{3}$$

where $Z_s = \sqrt{R^2 + (\omega_e L_s)^2}$; R is the total resistance which is the summation of the resistance of the machine, power switch device, and power cable.

From (3), it can be seen that the voltage constraint is a circle whose center point is $(\omega_e^2 L_s \psi_m / Z_s^2, \omega_e R_s \psi_m / Z_s^2)$ and the radius is V_m / Z_s. As the speed increases, the voltage limit circle shrinks. If the resistance is ignored or the machine speed is infinity, the center of the voltage limit circle is $(-i_c, 0)$, where i_c is the characteristic current. As illustrated in Figure 1, the speed range of the machine with MTPV control can be categorized into three distinct regions:

1. Region I

In the region I, the machine operates on the curve 'OA', aiming to achieve maximum torque per ampere (MTPA). Since the machine operates inside the current and voltage limit circle, i.e., $|\boldsymbol{I}_s| < I_m$ and $|\boldsymbol{V}_s| < V_m$, no flux-weakening control is required in this region.

2. Region II

The region II includes the curve 'AB' and the area within the closed curve 'OABCO'. On the curve 'AB', the machine operates on the intersection point of the voltage and current limit circles, i.e., $|\boldsymbol{V}_s| = V_m$ and $|\boldsymbol{I}_s| = I_m$. In the area 'OABCO', the machine operates on the voltage limit circle and inside the current limit circle, i.e., $|\boldsymbol{V}_s| = V_m$ and $|\boldsymbol{I}_s| < I_m$. In region II, the flux-weakening control is required to satisfy the voltage and current constraints.

3. Region III

In the region III, the machine operates on the MTPV curve 'BC' that inside the current limit circle, i.e., $|\boldsymbol{I}_s| < I_m$ and $|\boldsymbol{V}_s| = V_m$. In this region, the MTPV control strategy can be applied to maximize the torque capability and extend the operation speed range.

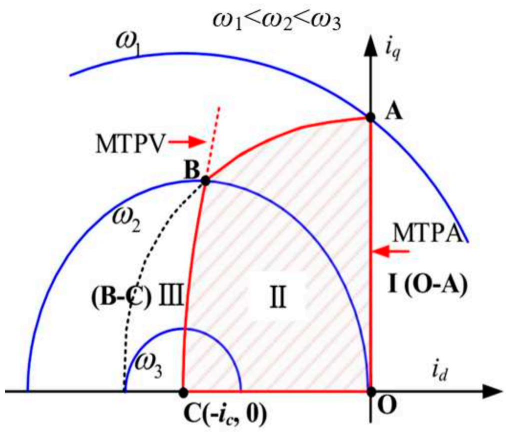

Figure 1. Operation regions. ω represents the electrical rotational speed. The relationship between the different speed regions is given by $\omega_1 < \omega_2 < \omega_3$, where ω_1, ω_2 and ω_3 correspond to the specific speed boundaries of the operational zones.

2.3. Control Strategies

Figure 2 shows the schematic of the control system, which is based on the conventional current vector control system using a dual current control structure that regulates the i_d and i_q currents.

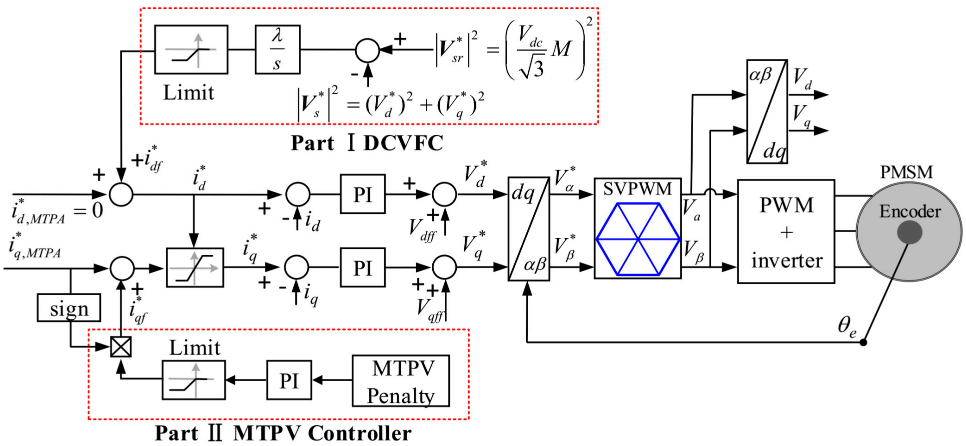

Figure 2. Schematic of the proposed flux-weakening control system.

In the region I, d- and q-axis current commands, denoted as $i^*_{d,MTPA}$ and $i^*_{q,MTPA}$, are determined based on the MTPA method. For a non-salient PMSM, $i^*_{d,MTPA}$ is zero in the region I while $i^*_{q,MTPA}$ is directly calculated, as it is proportional to the torque requirement.

In region II, the d-axis current voltage feedback controller (DCVFC) using a pure integrator is applied [14]. The expression for the demagnetizing d-axis current command is given by

$$i^*_{df} = \lambda \int (|\boldsymbol{V}^*_{sr}|^2 - |\boldsymbol{V}^*_s|^2)dt \tag{4}$$

where λ is the integration gain; i_{df}^* is the demagnetizing d-axis current command; $\boldsymbol{V^*_s}$ is the voltage command vector before the over modulation block, i.e., $(V_d^* + jV_q^*)$ in dq reference frame or $(V_\alpha^* + jV_\beta^*)$ in $\alpha\beta$ reference frame; $|\boldsymbol{V^*_{sr}}|$ is the voltage magnitude reference, i.e., $MV_{dc}/\sqrt{3}$, where M is the coefficient that can be used to adjust voltage magnitude reference. When $M \leq 1$, the system operates in the LMR. For the conventional minimum phase error over modulation (MPEOM), when $M = 2/\sqrt{3}$, the voltage magnitude can be extended to the hexagon boundary, at which condition the magnitude of the fundamental component is 0.6057 V_{dc}.

In the region III, the machine operates on the MTPV curve, which can be obtained at the tangent point of the voltage limit circle and constant torque curve. Therefore, the penalty function for the MTPV operation, i.e., P, can be defined as

$$P = \frac{1}{2}\left(\frac{\partial |\boldsymbol{V}_s|^2}{\partial i_d}\frac{\partial T_e}{\partial i_q} - \frac{\partial T_e}{\partial i_d}\frac{\partial |\boldsymbol{V}_s|^2}{\partial i_q}\right) \tag{5}$$

where the condition $P = 0$ represents the MTPV curve. The MTPV control strategy is realized by designing a feedback controller that drives the penalty function to zero. This feedback-based approach ensures that the system automatically transitions from the FW region to the MTPV region. The feedback controller continuously monitors the system's performance and makes real-time adjustments, seamlessly switching between the FW and MTPV regions, ensuring the machine operates efficiently on the MTPV curve. As shown in Part II of Figure 2, the q-axis current command is further modified by the output of a PI controller. The modified term, i.e., i_{qf}^*, can be expressed as

$$i^*_{qf} = sign(i^*_{q,MTPA})min(0, \frac{k_{pqf}s + k_{iqf}}{s}P) \tag{6}$$

where k_{pqf} and k_{iqf} are the proportional and integral gains of the PI controller. Therefore, the q-axis current command can be obtained as

$$i^*_q = sign(i^*_{q,MTPA})\min(\sqrt{I_m^2 - (i^*_d)^2}, \left|i^*_{q,MTPA} + i^*_{qf}\right|) \tag{7}$$

The combined FW and MTPV controllers ensure efficient motor operation at high speeds in the MTPV region. The FW controller weakens the flux to enable higher speeds within voltage limits, while the MTPV controller adjusts i_q to maximize torque for the given voltage.

3. Optimized MTPV Controller

3.1. Penalty Function for MTPV

At steady state, by referring (1) and (5), P can be derived in voltage and current form as

$$P = \begin{cases} P_v &= \omega_e V_q L_s + RV_d \\ P_c &= (i_d + i_c \frac{(\omega_e L_s)^2}{Z_s^2})Z_s^2 \end{cases} \tag{8}$$

where P_v and P_c represent the voltage and current forms of the penalty function, respectively.

According to (8) if the resistance is ignored, the MTPV curve can be simplified as $\omega_e V_q$ = 0 or $i_d = -i_c$, as shown in Figure 3. However, for the small power machine especially when the power cable is required, the ignoring of the resistance could cause a notable deviation of the current trajectory from the actual one.

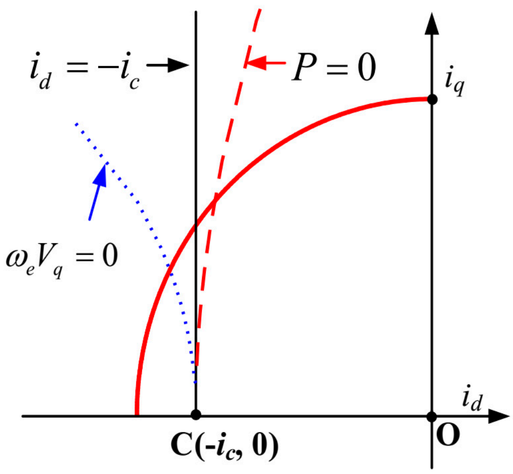

Figure 3. Current trajectory under different conditions.

Thus, when seeking the optimal current trajectory, it is advantageous to employ a resistance-weighted penalty function. A voltage-based penalty term, P_v, can be defined in terms of the d- and q-axis voltage commands, V_d and V_q. However, in the over-modulation region, the over-modulation stage induces ripple components in both V_d and V_q. Furthermore, the voltage commands are not purely steady-state: they also include dynamic components arising from the output of the current PI regulator. For example, within the LMR, the q-axis voltage command satisfies $V_q = V^*_q$ (see Figure 2). Consequently, the PI regulator output V^*_q is reintroduced into the q-axis current reference via the MTPV PI loop. Any high-frequency ripple on V^*_q is therefore propagated—and even amplified—by the cascaded PI controllers. Because classical PI controllers offer limited rejection of such high-frequency components, this amplification can induce oscillations and, in the worst case, destabilize the drive. In [22], a precede first order low pass filter is added to the MTPV controller to solve this problem, and the penalty function is revised to P_{vLpf}, i.e.,

$$P_{vLpf} = P_v \frac{\omega_c}{s + \omega_c} \tag{9}$$

where ω_c is the cut off frequency of the lower pass filter. However, the introduced low pass filter will limit the dynamics of the MTPV loop. In order to improve the dynamic performance, the penalty function without low pass filter is preferred.

Alternatively, the penalty function can also be expressed in the current form, i.e., P_c, in (8). Since the MTPV controller aims to plan the current command trajectory in the region III, i_d in P_c can be replaced by the d-axis current command $i_d{}^*$. In addition, as P_c = 0 represents the MTPV curve, the term Z_s^2 can be canceled out. Therefore, the penalty function in the current form can be revised as

$$P_c = i_d^* + i_c \frac{(\omega_e L_s)^2}{Z_s^2} \tag{10}$$

At the equilibrium point, the variation of the machine speed can be ignored due to the larger mechanical time constant when compared with the electrical time constant. Therefore, (10) implies that the variation of P_c mainly origins from the variation of $i_d{}^*$, i.e.,

$\Delta P_c = \Delta i_d^{\ *}$, where the prefix '$\Delta$' denotes their corresponding small signals. From the small signal point of view, in ΔP_c, only $\Delta i_d^{\ *}$ is the information required for the MTPV control. According to (6), in region III, the d-axis current command output by DCVFC will be directly transformed to the q-axis current command by the MTPV controller. Therefore, no extra filter is required, and better dynamics can be expected than that by using the voltage command feedback MTPV controller.

For easy comparison in the experimental section, the penalty function P_{vLpf} is divided by Z_s^2 to keep the same dimension as P_c in (10). The block diagrams of the MTPV controller by using voltage command feedback and current command feedback are shown in Figure 4a,b, respectively.

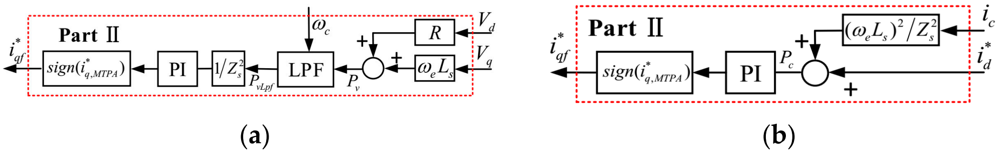

Figure 4. Block diagram of MTPV controllers. (**a**) Voltage command feedback controller. (**b**) Current command feedback controller.

Since the optimal current trajectory for the MTPV requires accurate parameters, in practice, this could be done by online parameter estimation. As the parameter estimation is out of the scope of this paper, it will not be discussed further. It should be noted that accurate parameters are only required to improve the steady-state performance. Therefore, the parameters used for the estimating P_c can be updated much slower than the dynamics of the MTPV loop. It means that the MTPV control and parameter estimation will not interfere with each other if the penalty term P_c is employed. In other words, the improvement of the dynamic performance and the steady performance can be done separately. In this paper, P_c is finally used as the penalty function for the MTPV control owing to its better dynamic performance.

3.2. MTPV Control Design

Due to the nonlinear behavior of the voltage loop in flux-weakening regions, the flux-weakening controller can be designed based on the linearized model. Therefore, considering the current, voltage, and torque constraints, and according to the different small signal behaviors, the operation modes in the flux-weakening region can be classified into three categories, as shown in Figure 5: mode A, where the machine operates on the current limit circle; mode B, where the machine operates along the constant torque curve; and mode C, where the machine operates on the MTPV curve.

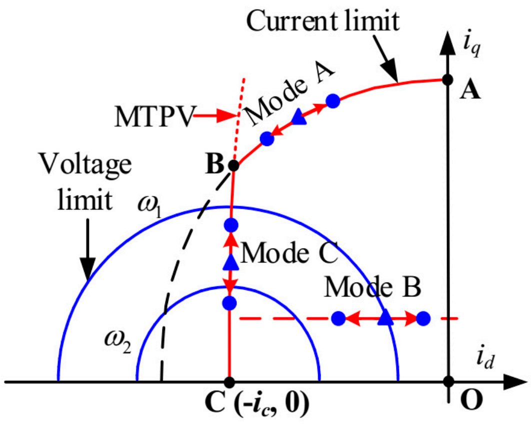

Figure 5. Operation modes with considering MTPV control.

Under different operation modes, the direction of current variation differs and can be characterized by the slope of the current trajectory, defined as $k = \Delta i_q/\Delta i_d$.

In region II, the MTPV controller is not activated, only the DCVFC is required. In region III, the DCVFC and MTPV controller are both involved in control, DCVFC is still an important part for the MTPV control. Therefore, DCVFC is analyzed first. Figure 6 shows the equivalent linearized model of the voltage loop with DCVFC [14]. In Figure 6, $C_{df}(s)$, $T_i(s)$ and $G_{df}(s)$ are the transfer functions of the integral controller, the equivalent current loop, and the control plant, respectively. $C_{df}(s)$, $T_i(s)$ and $G_{df}(s)$ can be expressed as

$$C_{df}(s) = \frac{\lambda}{s} \tag{11}$$

$$T_i(s) = \frac{\omega_c}{s+\omega_c} \tag{12}$$

$$G_{df}(s) = \frac{\Delta|\boldsymbol{V}_s^*|^2}{\Delta i_d} \approx \frac{\Delta|\boldsymbol{V}_s|^2}{\Delta i_d} = 2V_d^0\frac{\Delta V_d}{\Delta i_d} + 2V_q^0\frac{\Delta V_q}{\Delta i_d} = bs + a \tag{13}$$

where ω_c is the bandwidth of the current loop; the variables with superscript '0' denote their steady-state values on the equilibrium point.

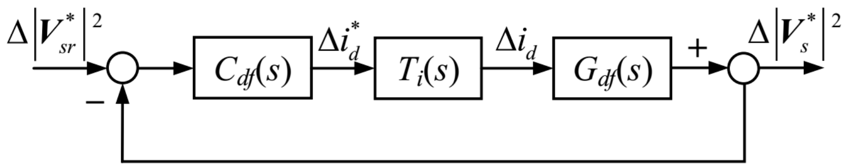

Figure 6. Linearized model of voltage loop with DCVFC.

Assuming Δi_q = kΔi_d, a and b can be expressed as

$$\begin{cases} a = 2\omega_e^0(V_q^0 L_s - V_d^0 k L_s) + 2R_s(V_d^0 + V_q^0 k) \\ b = 2(V_d^0 L_s + V_q^0 L_s k) \end{cases} \tag{14}$$

Therefore, the close-loop transfer function of the voltage loop with DCVFC can be expressed as

$$\Phi(s) = \frac{\omega_c \lambda(bs+a)}{s^2 + \omega_c(1+b\lambda)s + \omega_c \lambda a} \tag{15}$$

According to the Routh stability criterion, the stable condition of the voltage loop with DCVFC is

$$\begin{cases} a\lambda > 0 \\ 1 + b\lambda > 0 \end{cases} \tag{16}$$

The details of selection of λ can be referred to Appendix A. When the machine operates in the region III, the operation mode B that is activated by the DCVFC cooperates with the mode C that is activated by the MTPV controller. For the DCVFC, the voltage loop can be analyzed in mode B. Since i_q remains constant in mode B, the slope k equals zero, and the coefficients a and b can be derived accordingly as

$$\begin{cases} a|_{modeB} = 2(\omega_e^0 V_q^0 L_s + R V_d^0) \\ b|_{modeB} = 2V_d^0 L_d \end{cases} \tag{17}$$

where $a|_{modeB}$ and $b|_{modeB}$ denote the values of a and b in mode B. At the equilibrium point, it can be seen that $a|_{modeB} = 2P_v$. Therefore, in the region III, $a|_{modeB} = 0$, which means that the voltage loop with DCVFC cannot maintain stable in this region and the MTPV control strategy has to be applied.

Furthermore, the equivalent linearized model of MTPV loop is shown in Figure 7. In Figure 7, $C_{qf}(s)$ and $G_{qf}(s)$ are the transfer functions of the PI controller and the control plant of the MTPV loop, respectively; δ is the reference of MTPV loop, which is an infinitesimal value. $C_{qf}(s)$ and $G_{qf}(s)$ can be obtained as

$$C_{qf}(s) = \frac{k_{pqf}s + k_{iqf}}{s} \tag{18}$$

$$G_{qf}(s) = -\frac{\Delta P_c}{\Delta i_q^*} \tag{19}$$

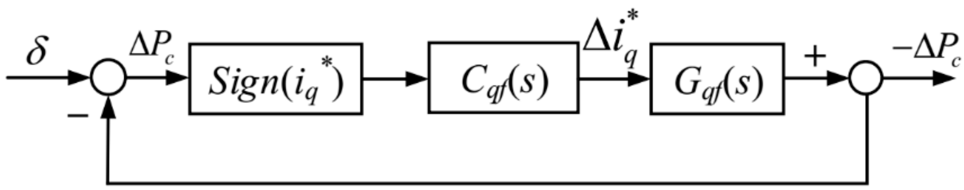

Figure 7. Block diagram of linearized model of MTPV Loop.

According to (10), $\Delta P_c = \Delta i^* d$, $G_{qf}(s)$ can be rewritten as

$$G_{qf}(s) = -\frac{\Delta i_d^*}{\Delta i_q^*} \tag{20}$$

Since $\Delta i^* d$ origins from DCVFC, $G_{qf}(s)$ can be reconstructed as

$$G_{qf}(s) = -\frac{\Delta i_d^*}{\Delta |\boldsymbol{V}_s^*|^2} \frac{\Delta |\boldsymbol{V}_s^*|^2}{\Delta i_q^*} \tag{21}$$

In region III, the term $\Delta i_d^* / \Delta |\boldsymbol{V}_s^*|^2$ can be obtained from Figure 6. When a = 0, it can be derived as

$$\frac{\Delta i_d^*}{\Delta |\boldsymbol{V}_s^*|^2} = -\frac{\lambda}{s} \frac{(s + \omega_c)}{(s + \omega_c(1 + b|_{modeB}\lambda))} \tag{22}$$

According to Appendix A, $b|_{modeB}\lambda \approx 0$ in region III, and $\Delta i_d^* / \Delta |\boldsymbol{V}_s^*|^2 \approx -\lambda_I / s$. In addition, $\Delta |\boldsymbol{V}_s^*|^2 / \Delta i_q^*$ can be derived as

$$\frac{\Delta |\boldsymbol{V}_s^*|^2}{\Delta i_q^*} = 2V_d^0 \frac{\Delta V_d^*}{\Delta i_q^*} + 2V_q^0 \frac{\Delta V_q^*}{\Delta i_q^*} \tag{23}$$

Moreover, since V_q^0 is close to zero, and $V_d^0 = -V_m sign(\omega_e^0 i_q^*)$ due to that $i_d \approx -i_c$ in region III, $\Delta |\boldsymbol{V}_s^*|^2 / \Delta i_q^*$ can be approximated as

$$\begin{aligned} &\frac{\Delta |\boldsymbol{V}_s^*|^2}{\Delta i_q^*} \approx -2V_m \frac{\Delta V_d^*}{\Delta i_q^*} sign(\omega_e^0 i_q^*) \\ &\approx -2V_m \frac{\Delta V_d}{\Delta i_q} \frac{\Delta i_q}{\Delta i_q^*} sign(\omega_e^0 i_q^*) = -2sign(i_q^*) V_m |\omega_e^0| L_s T_i(s) \end{aligned} \tag{24}$$

In consequence, the control plant of the MTPV loop can be derived as

$$G_{qf} = K_{qf}\frac{1}{s}T_i(s)sign(i_q^*) \tag{25}$$

where $K_{qf} = 2V_m|\omega_e^0|L_s\lambda_I$. Equation (25) explains that a pure integral controller is not applicable for the MTPV controller, as the system could oscillate due to the resultant origin pole of the close-loop transfer function. Therefore, a PI controller can be adopted, which can ensure the stability in region III. The open-loop transfer function of the MTPV loop with PI controller, i.e., $G_{oqf}(s)$ can be derived and simplified as

$$G_{oqf} = K_{qf}\frac{k_{pqf}s + k_{iqf}}{s}\frac{1}{s}T_i(s) \tag{26}$$

It is reasonable to make a further simplification of (26) by approximating $T_i(s)$ as a unity gain if the MTPV loop is tuned with the bandwidth much lower than the current bandwidth. Therefore, the close-loop function of the MTPV loop can be obtained as

$$\frac{-P_c}{\delta} = \frac{(k_{pqf}K_{qf}s + K_{qf}k_{iqf})}{s^2 + k_{pqf}K_{qf}s + K_{qf}k_{iqf}} \tag{27}$$

As a second order system, the control parameters can be tuned as

$$k_{pqf} = \frac{2\xi\omega_{Nqf}}{K_{qf}} = \frac{2\omega_{Nqf}}{K_{qf}}, k_{iqf} = \frac{\omega_{Nqf}^2}{K_{qf}} \tag{28}$$

where ω_{Nqf} is the selected natural frequency, ξ is selected damping factor which is set at 1 in the experiments.

3.3. Over Modulation Improvement

Figure 8 illustrates voltage synthesis under MPEOM in both linear and over-modulation regions. In the linear region, the reference voltage vector V_s can be accurately synthesized without distortion. However, in the over-modulation region, only vectors located within the hexagonal boundary are fully realizable. Any reference vector extending beyond this limit is clipped to the hexagon perimeter while preserving its direction. Figure 9 presents the normalized spectral content of the α-axis voltage with respect to V_{dc} for modulation indices M = 0.9 and M = 1.1. The amplitude of the fundamental component serves as an indicator of DC-link voltage utilization.

The over-modulation region demonstrates improved utilization of the DC-link voltage compared to the LMR. However, this benefit comes at the cost of reduced voltage control margin and increased harmonic content. As a result, voltage saturation becomes more prominent, negatively impacting current regulation and potentially causing instability. To mitigate this issue, the flux-weakening control scheme utilizes a d-axis current reference generated via the DCVFC and a q-axis current reference provided by the MTPV controller. Ensuring rapid and stable current dynamics is thus critical for maintaining system stability within the flux-weakening region.

In the over modulation region, the VVM shows a good option for improving the current dynamics, which is firstly proposed in [9] and applied in region II. In this paper, the VVM will be applied in both region II and region III to improve the system stability in over modulation region. The working principle of the VVM is quite simple, which will be briefly introduced as follows.

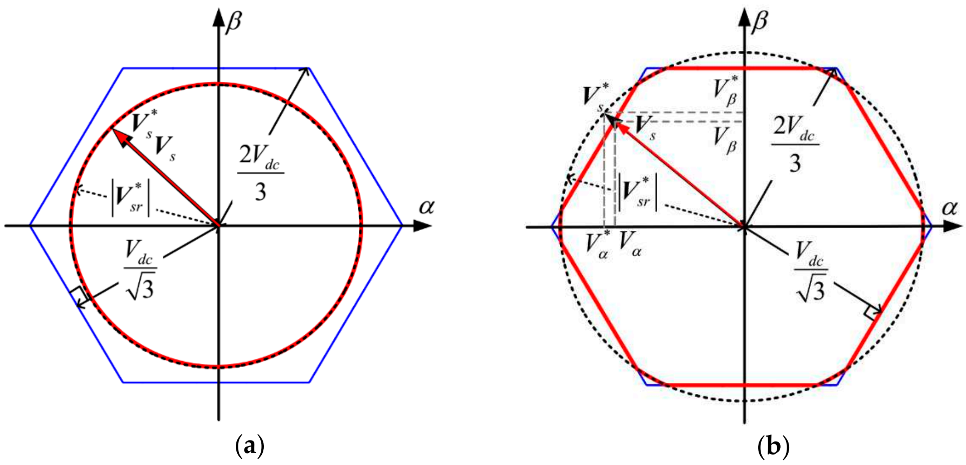

Figure 8. Voltage synthesis with MPEOM. (**a**) Linear modulation range (M = 0.9). (**b**) Over modulation range (M = 1.1).

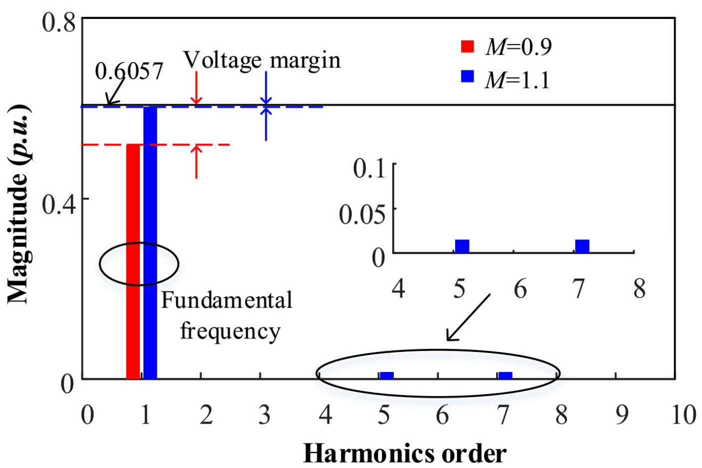

Figure 9. Voltage spectra with MPEOM when M = 0.9 and M = 1.1.

Since the inductive voltage drop on the inductance can be approximated as

$$\begin{cases} L_s \frac{di_d}{dt} \approx V_d + \omega_e L_s i_q \\ L_s \frac{di_q}{dt} \approx V_q - \omega_e (L_s i_d + \psi_m) \end{cases} \quad (29)$$

The right side of (29) represents the voltage margin in d- and q-axes that can be created. When V_d and V_q are already limited on the hexagon boundary, the only way to increase the voltage margin is to utilize the coupling term between d- and q-axes. For example, when $\omega_e > 0$, decreasing i_d can be realized by decreasing i_q, and therefore decreasing V_q; increasing i_q can be realized by decreasing i_d, and therefore decreasing V_d. By utilizing this coupling feature between d- and q-axes, the voltage command vector can be modified as

$$\boldsymbol{V}_{sm}^* = \boldsymbol{V}_s^* + j\boldsymbol{V}_{sme}^* \mathrm{sign}(\omega_e) \quad (30)$$

where $\boldsymbol{V}^*_{sme} = \boldsymbol{V}^*_s - \boldsymbol{V}_{stmp}$ is the temporal voltage error vector between the input voltage command vector $\boldsymbol{V}^*_s$ and temporal voltage vector $\boldsymbol{V}_{stmp}$, as shown in Figure 10; $\boldsymbol{V}^*_{sm}$ is the new modified voltage vector, i.e., $\boldsymbol{V}^*_{dm} + j\,\boldsymbol{V}^*_{qm}$.

Figure 11 presents the scalar-based implementation of the VVM in block diagram form. In this configuration, the voltage commands generated by the current controllers, V_d^*

and V_q^* are modified to V_{dm}^* and V_{qm}^*, through the VVM. These modified commands are subsequently processed by the MPEOM scheme before being applied to the inverter.

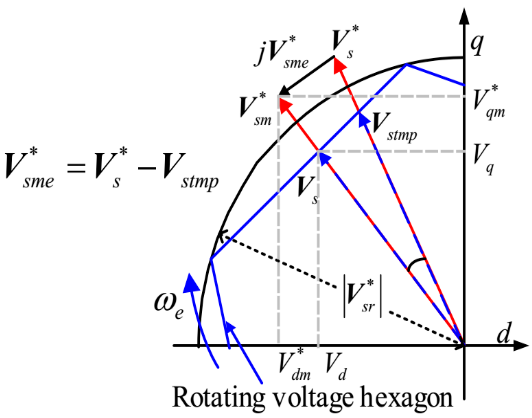

Figure 10. Voltage vector modifier (VVM).

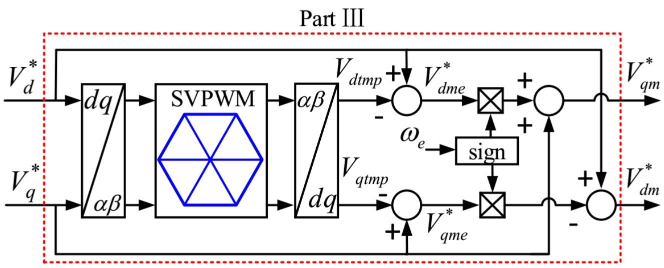

Figure 11. Block diagram of VVM.

The whole control diagram with MTPV controller and the VVM can be seen in Figure 12. Since the temporal voltage error vector V^*_{sme} only exists in the over modulation region, the VVM will not influence the steady-state performance in the LMR.

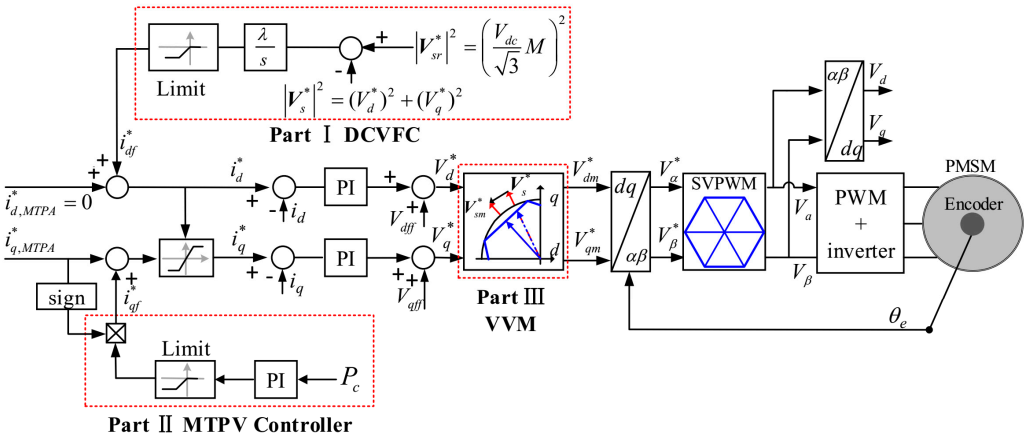

Figure 12. Schematic of improved feedback type flux-weakening control system.

4. Experimental Verification

Experimental validation is carried out using a non-salient pole PMSM controlled via a dSPACE-based setup. The inverter employs IRFH7440-type MOSFETs as switching devices. Due to its negligible value relative to the motor resistance, the drain-source resistance (below 2.4 mΩ) is disregarded in analysis. The system operates at a PWM switching frequency of 10 kHz, with the current control loop bandwidth configured at 1200 rad/s. A visual overview of the experimental setup is provided in Figure 13.

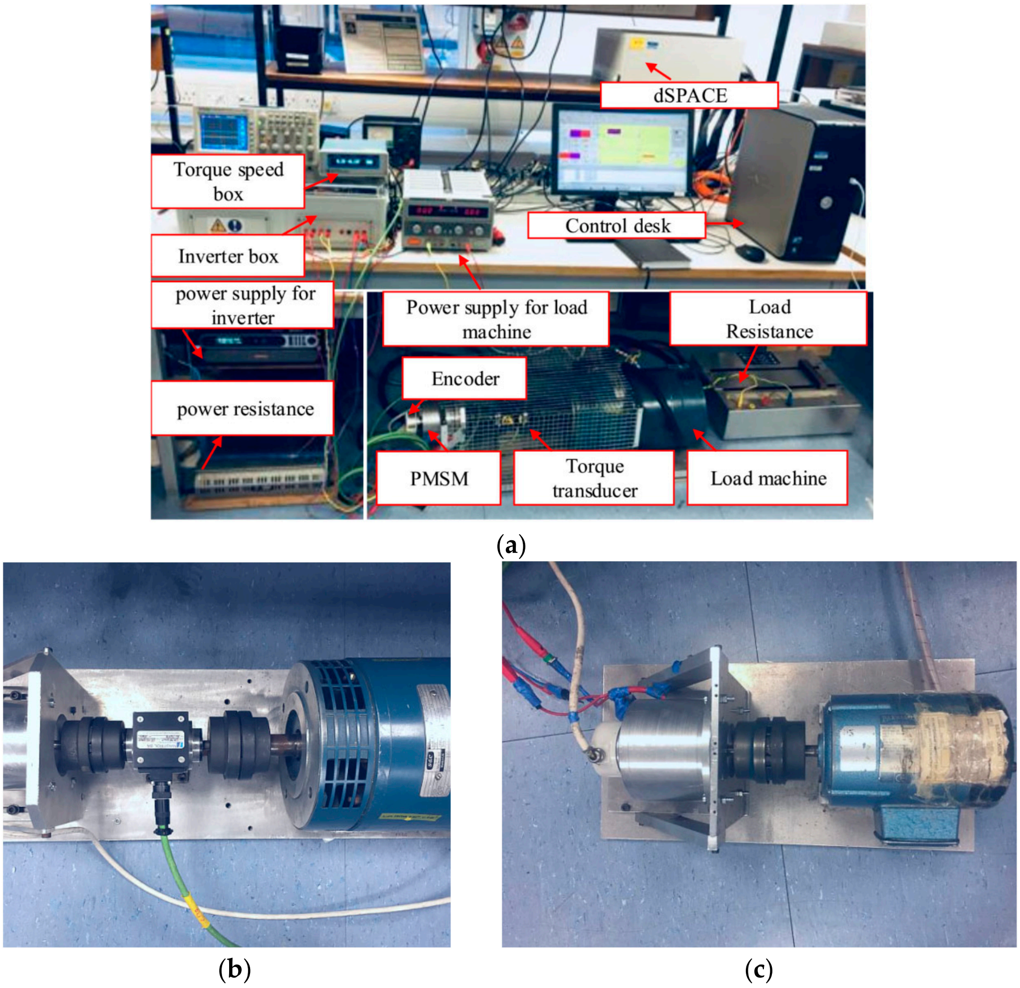

Figure 13. Real drive system based on dSPACE platform and two test rigs. (**a**) dSPACE platform. (**b**) Test rig I with big inertia and torque transducer. (**c**) Test rig II with small inertia.

As shown in Figure 13, Test Rig I is equipped with a high-inertia load of 0.012 kg·m^2 and incorporates a torque transducer for steady-state performance evaluation. In contrast, Test Rig II features a lower inertia of 0.001 kg·m^2, making it suitable for assessing transient behavior. Detailed specifications of the machine and drive system are provided in Table 1. For dynamic testing, data acquisition is conducted at a sampling rate of 1 kHz.

Table 1. Machine and drive parameters.

Parameters	Value
Phase resistance (R_s)	0.25 Ω
Synchronous inductance (L_s)	1.7 mH
PM-flux linkage (ψ_m)	10 mWb
Number of pole pairs	10
DC link voltage (V_{dc})	14 V
Current limit (I_m) when i_{cn} = 1	7.35 A
Current bandwidth (ω_{cc})	1200 rad/s
Rated speed (n*)	1000 rpm
Cable resistance	0.1 Ω
PWM switching frequency	10 Hz

The following experimental results begin with an evaluation of steady-state performance using Test Rig I, highlighting the benefits of incorporating resistance effects within the MTPV region. Subsequently, the dynamic behavior of the system employing a current command feedback MTPV controller is examined and compared against its voltage command feedback counterpart. Finally, system stability in the over-modulation region is analyzed under conditions with and without the implementation of the VVM.

4.1. Steady-State Performance

Figure 14 shows the steady-state performance for M = 0.9M under three distinct MTPV penalty function scenarios: $V_q\omega_e = 0$ (case 1) $i_d = -i_c$ (case 2) and $P_c = 0$ (case 3). Cases 1 and 2 correspond to implementations where the impact of resistance is neglected, using voltage- and current-based forms, respectively. In contrast, Case 3 incorporates the resistance effect into the penalty function. The resistance value considered in P_c is the total resistance of the system, set to 0.35 Ω.

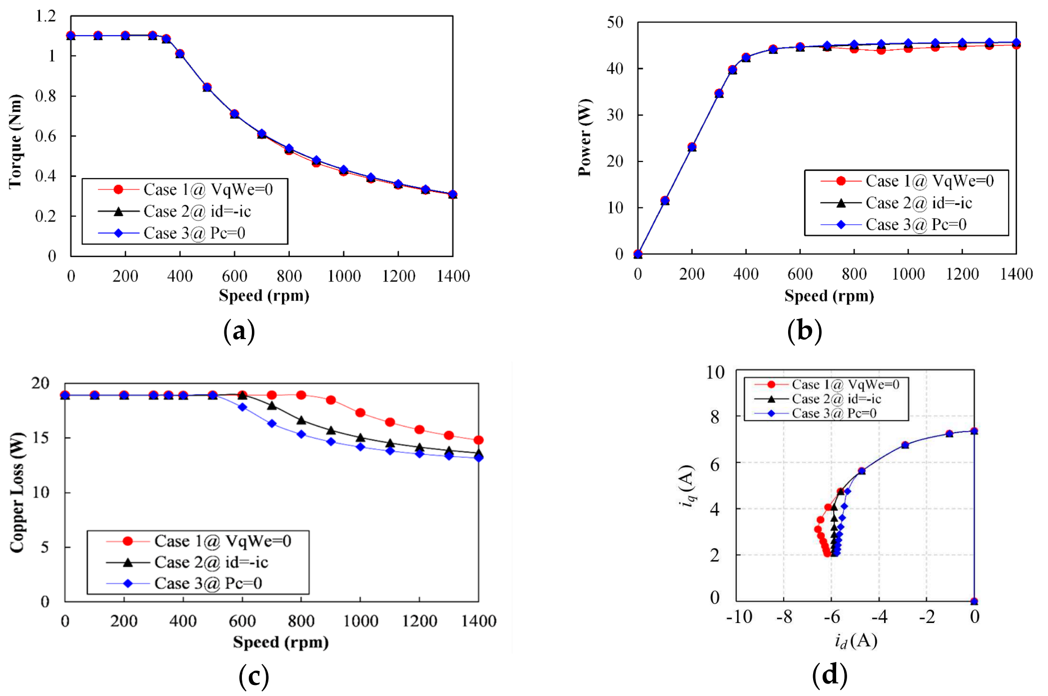

Figure 14. Steady-state performance under different cases. (**a**) Torque-speed curve. (**b**) Power-speed curve. (**c**) Copper loss speed curve. (**d**) Current trajectories.

Figure 14a,b show the torque speed curve and power speed curve, respectively, under three cases. Although the variations in output torque and power among the three test cases are relatively small, Case 3 consistently delivers marginally higher values compared to Cases 1 and 2 when the machine speed exceeds approximately 650 rpm. Conversely, Case 1 produces the lowest torque and power across the range. As illustrated in Figure 14c, Case 3 also exhibits the lowest copper losses among the three scenarios. At 900 rpm, the copper loss in Case 3 is approximately 25% lower than that of Case 1. Figure 14d further reveals that Case 3—where resistance is taken into account—achieves the smallest current magnitude, particularly near the operating region where the system transitions from mode A to mode C, thereby contributing to the reduced copper loss. Additionally, Case 3 enters the MTPV region earlier than the others. Accurate tracking of the MTPV trajectory during dynamic transitions may further enhance the system's dynamic response.

4.2. Dynamic Performance with Different MTPV Controllers

The dynamic responses of the system under voltage and current command feedback MTPV control schemes are evaluated by applying a step input of $i^*_{q,MTPA}$ = 7.35A with a modulation index M = 0.9. Figure 15 shows the dynamic behavior of the system using the voltage command feedback controller under varying PI parameter settings. In Figure 15a, noticeable oscillations occur in the absence of a low-pass filter. By setting ω_{Nqf} = 50 rad/s and ω_c = 600 rad/s, the system maintains stable behavior, as depicted in Figure 15b, though an evident overshoot appears in both the current response and the and P_{vLpf} profile. When the cutoff frequency ω_{Nqf} is increased further—as shown in Figure 15c—oscillatory behavior reemerges, indicating a loss of system stability.

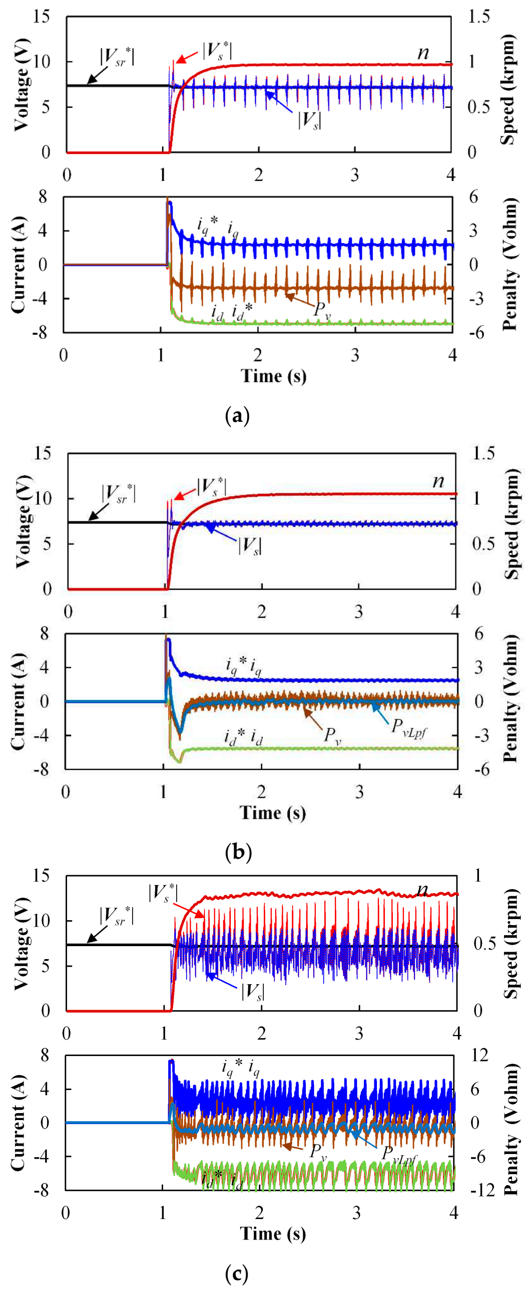

Figure 15. Dynamic performance with voltage command feedback MTPV controller. (**a**) Without low pass filter and ω_{Nqf} = 50 rad/s. (**b**) With low pass filter ω_c = 600 rad/s and ω_{Nqf} = 50 rad/s. (**c**) With low pass filter ω_c = 600 rad/s and ω_{Nqf} = 100 rad/s.

Figure 16 shows the dynamic performance by using the current command feedback MTPV controller under different PI control parameters. It can be seen that the system can operate stably when ω_{Nqf} are 50 rad/s and 200 rad/s, as shown in Figure 16a,b, respectively. Figure 17 illustrates the current trajectories when ω_{Nqf} = 50 rad/s and 200 rad/s. when ω_{Nqf} = 50, as shown in Figure 17a, although the current shows overshoot when approaching MTPV curve, this overshoot is much less when ω_{Nqf} increases to 200 rad/s. As a result, better speed dynamics can be obtained, which can be seen in Figure 18.

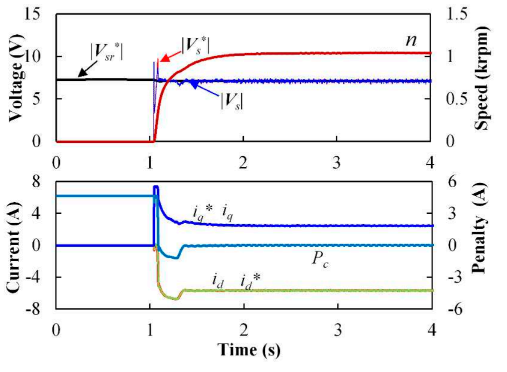

Figure 16. Dynamic performance with current command feedback MTPV controller. (**a**) ω_{Nqf} = 50 rad/s. (**b**) ω_{Nqf} = 200 rad/s.

From the foregoing analysis, the pure integral MTPV controller can hardly maintain the stability in the MTPV region. In order to demonstrate this phenomenon, Figure 19 shows one of the oscillation cases when the integral gain is tuned by disabling the proportional controller while ω_{Nqf} = 50 rad/s.

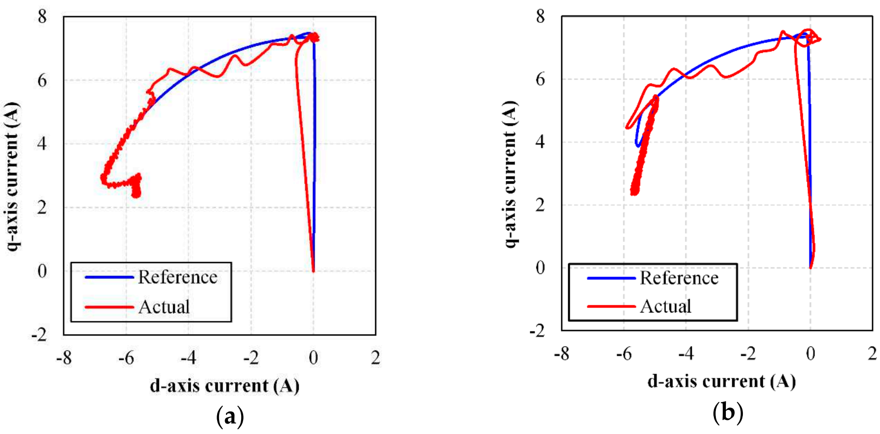

Figure 17. Dynamic current trajectories with current command feedback MTPV controller. (**a**) ω_{Nqf} = 50 rad/s. (**b**) ω_{Nqf} = 200 rad/s.

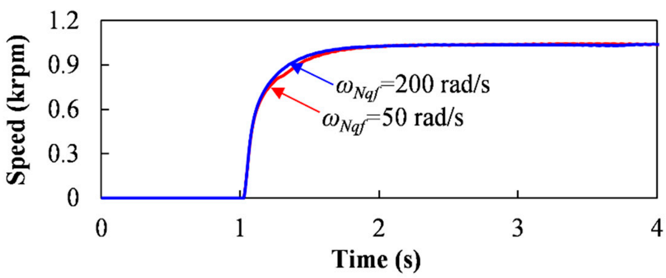

Figure 18. Speed dynamics of current command feedback MTPV controller under different control parameters.

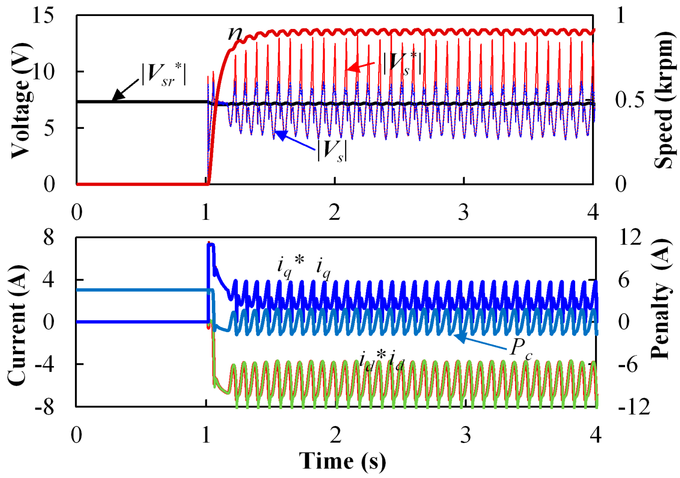

Figure 19. Dynamic performance with current command feedback MTPV controller (integral controller).

4.3. Stability in over Modulation Region

When M = 1.15, the system stabilities are compared under the conditions with and without VVM. By changing q-axis current command from 1A to 2A at 2 seconds, the machine accelerates from region I to region II, and then to region III. Figure 20a shows the system performance without VVM. It can be seen that both current and voltage oscillate in the flux-weakening regions (region II and region III). However, as shown in Figure 20b, with the VVM, the system stability in flux-weakening region is remarkably improved. It should be noted that the ripples of $|V_s|$ in Figure 20b is caused by the limit boundary of the over modulation block.

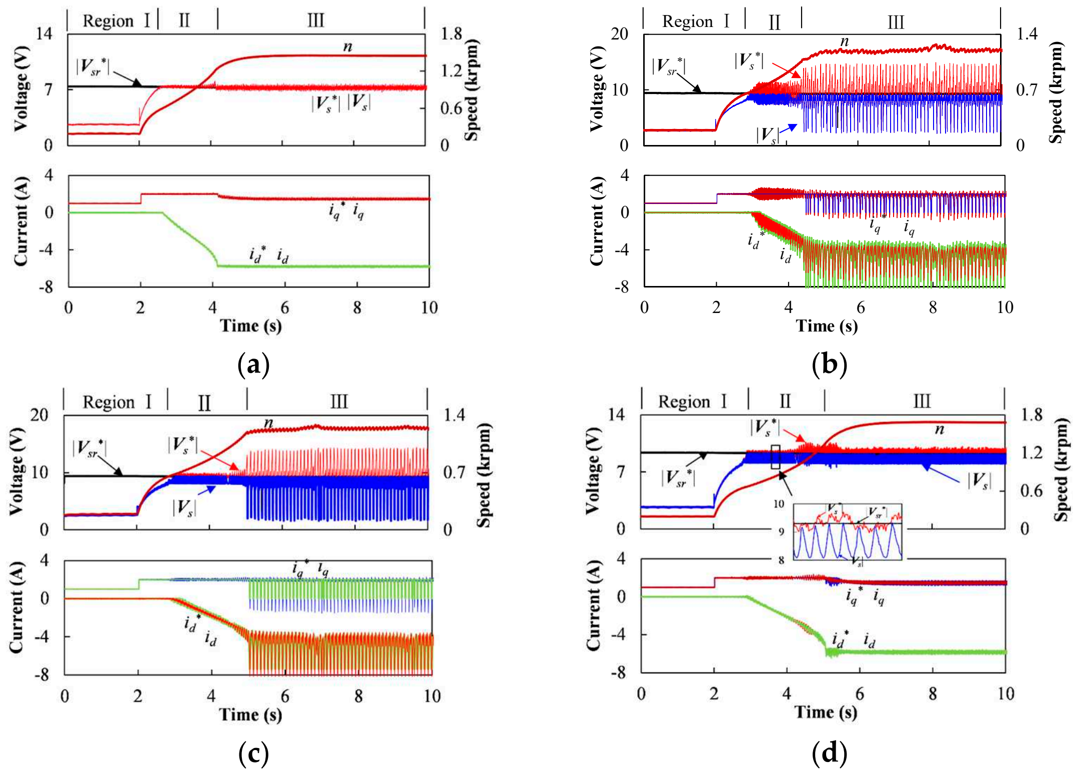

Figure 20. System performance in over modulation region (M = 1.15). (**a**) With only conventional DCVFC, M = 0.9. (**b**) With only conventional DCVFC, M = 1.15. (**c**) With added CRM and VRM, M = 1.15. (**d**) With added VVM, M = 1.15.

5. Conclusions

This paper investigates and improves a feedback-oriented flux-weakening control scheme for a non-salient PMSM, with particular emphasis on its operation in the MTPV region. To improve steady-state performance—particularly in low-power machines—the effect of stator resistance has been incorporated into the control framework. A comparative study of two MTPV controller structures, namely voltage-command and current-command feedback controller, has been conducted. Additionally, design considerations for a PI-based MTPV controller have been addressed with respect to maintaining system stability in the MTPV region. To further enhance system robustness in both over-modulation and flux-weakening regions, a VVM is employed. Theoretical analysis and experimental validation confirm the effectiveness of the proposed methods, demonstrating that:

1. The steady-state performance in the MTPV region can be improved by considering the resistance especially for the small power machine;
2. The current command feedback MTPV controller can obtain better dynamics than the voltage command feedback controller;
3. A PI MTPV controller is preferred as the pure integral MTPV controller can hardly maintain stability in the MTPV region;
4. The stability in the over modulation region under different flux-weakening regions (region II and region III) can be improved with VVM while the dual current control structure can still be preserved.

Author Contributions: Conceptualization, Z.Z. and C.W.; methodology, C.W. and Z.Z.; formal analysis, C.W.; investigation, C.W.; resources, Z.Z.; writing—original draft preparation, C.W. and Z.Z.; writing—review and editing, Z.Z., L.X., X.W. and K.L.; supervision, Z.Z.; project administration, Z.Z.; funding acquisition, Z.Z. All authors have read and agreed to the published version of the manuscript.

Funding: This work was supported by the Midea Group, China, under Grant No. R/157532-11-1.

Data Availability Statement: The original contributions presented in the study are included in the article, further inquiries can be directed to the corresponding author.

Conflicts of Interest: The authors declare that they have no conflicts of interest. The funder had no role in the design of the study; in the collection, analyses, or interpretation of data; in the writing of the manuscript; or in the decision to publish the results.

Appendix A

For the DCVFC, the control parameter λ can be tuned according to (15), which is a typical second order system. Since this question has been addressed by only considering the machine without MTPV region, the same method will be adopted here by including the MTPV region.

In mode A, the characteristic equation of (15) can be derived as

$$q(s) = s^2 + \omega_{cc}\left(1 - \frac{\omega_{mI}}{\omega_b}\sigma\right)s + \omega_{cc}\omega_{mI} \tag{A1}$$

where ω_{mI}, ω_b and σ are

$$\omega_b = V_m/(L_s I_m) \tag{A2}$$

$$\omega_{mI} = 2\lambda\omega_e^0 L_s \omega_e^0 L_s i_c \tag{A3}$$

$$\sigma = (1/i_{cn} + i_{dn})/(\omega_{en} i_{qn}) \tag{A4}$$

where i_{dn} and i_{qn} are the ${i_d}^0$ and ${i_q}^0$ normalized by I_m respectively; i_{cn} is i_c normalized by I_m; ω_{en} is ${\omega_e}^0$ normalized by ω_b; σ is an introduced normalized value and can be seen as a non-dimensional coefficient which varies with the operation points.

According to (A1), the damping factor ξ can be calculated as

$$\xi = \sqrt{\omega_c/(4\omega_{mI})}\left(1 - \frac{\omega_{mI}}{\omega_b}\sigma\right) \tag{A5}$$

It can be seen that ξ is inversely proportional to σ, the system can be designed on the operation point where σ is maximum. For the controller design, the resistance in the flux-weakening region can be ignored. Therefore, by considering the voltage and current constraints in the normalized form, i.e.,

$$\begin{cases} i_{dn}^2 + i_{qn}^2 = 1 \\ i_{qn}^2 + (i_{dn} + i_{cn})^2 = \frac{1}{\omega_{en}^2} \end{cases} \tag{A6}$$

σ can be plotted against i_{dn} for a given i_{cn}. As shown in Figure A1 when i_{cn} = 0.8 (for the machine in this paper), although σ could be positive infinity when i_{dn}= -1 in the motoring condition, this extreme condition can be reasonably ignored as the system will transfer to the mode C when $i_{dn} \approx -0.8$.

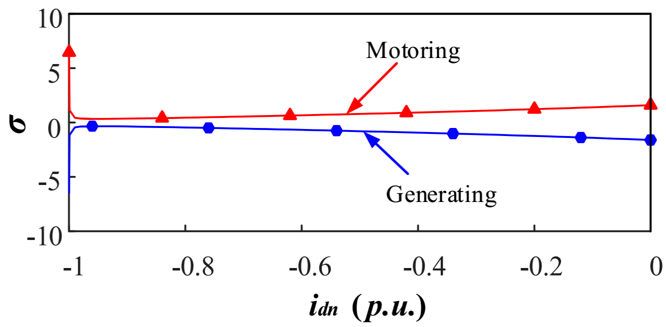

Figure A1. Variation of σ against i_{dn} when i_{cn} = 0.8.

According to (A5), if ξ is selected at critical damping condition (ξ = 1) at operation point when $\sigma = \sigma_s$, ω_{mI} can be approximated as

$$\omega_{vI} = \frac{\omega_c}{4}\frac{1}{\frac{\sigma_s}{2}\frac{\omega_c}{\omega_b} + 1} \tag{A7}$$

where σ_s can be set according to Figure A1. In this paper, σ_s is set at 2, which is larger than most of σ at different operation points.

Therefore, with the obtained ω_{mI}, λ in mode A can be derived as

$$\lambda|_{ModeA} = \frac{\omega_{mI}}{2\omega_e^0 L_s \omega_e^0 L_s i_c} = \frac{\omega_m}{2|\omega_e^0| L_s V_m}, \omega_m = \omega_{mIA} \tag{A8}$$

where $\omega_{mIA} = \omega_{mI}/(|\omega_{en}| i_{cn})$; $\lambda|_{modeA}$ denotes λ tuned in mode A.

In mode B, the Routh stable criterion requires that 1 + $b\lambda$ > 0 and $a\lambda$ > 0. The worst condition happens when V_d^0 is minimum, i.e., $V_d^0 = -V_m$, which defines the minimum stable range for the control parameter λ. Assuming that λ is tuned so that 1 + $b\lambda$ >0.5 at the worst condition, the control parameter λ in mode B can be set as

$$\lambda|_{ModeB} = \frac{\omega_m}{2|\omega_e^0| L_s V_m}, \omega_m \le \omega_{mIB} \tag{A9}$$

where $\omega_{mIB} = 0.5|\omega_e^0|$; $\lambda|_{modeB}$ denotes λ tuned in mode B.

In addition, it should be noted that ω_{mIA} is obtained in mode A and is inversely proportional to the machine speed. When system transfers to mode C, ω_{mIA} will be too small if the machine speed goes too high. Therefore, the minimum ω_{mIA} can be obtained at the operation point when the system transfers to mode C, and it can be approximately obtained when $i_{dn} = -i_{cn}$, i.e., $\omega_{mI}/1.3$ for $i_{cn} = 0.8$. Therefore, by considering mode C, ω_{mIA} can be further revised as

$$\omega_{mIA} = \max\left\{\frac{\omega_{mI}}{0.8|\omega_{en}|}, \frac{\omega_{mI}}{1.3}\right\} \tag{A10}$$

Finally, the control parameter λ can be set as

$$\lambda = \frac{\omega_m}{2|\omega_e^0|L_s V_m}, \omega_m = \min\{\omega_{mIA}, \omega_{mIB}\} \tag{A11}$$

Since the MTPV controller is tuned in mode C (region III), where ω_{mIA} is much smaller than ω_{mIB}, according to (17), $b|_{modeB}\lambda$ can be approximated as zero for the MTPV controller design.

References

1. Lin, Y.-S.; Yang, C.-W.; Liaw, C.-M.; Chiang, C.-L.; Liu, Y.-G.; Wang, C.-C. Development and Control of PMSM Drive with Improved Performance over Wide Speed and Load Ranges. *IEEE Access* **2024**, *12*, 97154–97170. [CrossRef]
2. Kim, J.-M.; Sul, S.-K. Speed Control of Interior Permanent Magnet Synchronous Motor Drive for the Flux Weakening Operation. *IEEE Trans. Ind. Appl.* **1997**, *33*, 43–48. [CrossRef]
3. Morimoto, S.; Takeda, Y.; Hirasa, T.; Taniguchi, K. Expansion of Operating Limits for Permanent Magnet Motor by Current Vector Control Considering Inverter Capacity. *IEEE Trans. Ind. Appl.* **1990**, *26*, 866–871. [CrossRef]
4. Eldeeb, H.; Hackl, C.M.; Horlbeck, L.; Kullick, J. A Unified Theory for Optimal Feedforward Torque Control of Anisotropic Synchronous Machines. *Int. J. Control* **2017**, *91*, 2273–2302. [CrossRef]
5. Miguel-Espinar, C.; Heredero-Peris, D.; Villafafila-Robles, R.; Montesinos-Miracle, D. Review of Flux-Weakening Algorithms to Extend the Speed Range in Electric Vehicle Applications with PM Synchronous Machines. *IEEE Access* **2023**, *11*, 22961–22981. [CrossRef]
6. Kwon, T.-S.; Sul, S.-K. Novel Antiwindup of a Current Regulator of a Surface-Mounted Permanent-Magnet Motor for Flux-Weakening Control. *IEEE Trans. Ind. Appl.* **2006**, *42*, 1293–1300. [CrossRef]
7. Wang, C.; Zhu, Z.Q.; Zhan, H. Adaptive Voltage Feedback Controllers on Nonsalient Permanent Magnet Synchronous Machine. *IEEE Trans. Ind. Appl.* **2020**, *56*, 1529–1542. [CrossRef]
8. Nalepa, R.; Orlowska-Kowalska, T. Optimum Trajectory Control of the Current Vector of a Nonsalient-Pole PMSM in the Field-Weakening Region. *IEEE Trans. Ind. Electron.* **2012**, *59*, 2867–2876. [CrossRef]
9. Kwon, T.-S.; Choi, G.-Y.; Kwak, M.-S.; Sul, S.-K. Novel Flux-Weakening Control of an IPMSM for Quasi-Six-Step Operation. *IEEE Trans. Ind. Appl.* **2008**, *44*, 1722–1731. [CrossRef]
10. Maric, D.S.; Hiti, S.; Stancu, C.C.; Nagashima, J.M.; Rutledge, D.B. Two Flux Weakening Schemes for Surface-Mounted Permanent-Magnet Synchronous Drives. *IEEE Trans. Ind. Electron.* **1999**, *2*, 673–678. [CrossRef]
11. Tursini, M.; Chiricozzi, E.; Petrella, R. Feedforward Flux-Weakening Control of Surface-Mounted Permanent-Magnet Synchronous Motors Accounting for Resistive Voltage Drop. *IEEE Trans. Ind. Electron.* **2010**, *57*, 440–448. [CrossRef]
12. Lu, K.; Zhu, Z.Q. Comparative Stability Analysis of IPMSM and SPMSM Machines Under Flux-Weakening Control. In Proceedings of the International Conference on Electrical Machines (ICEM) 2024, Torino, Italy, 1–4 September 2024; pp. 1–7. [CrossRef]
13. Jing, R.; Ding, D.; Zhang, G.; Wang, Q.; Wang, G.; Xu, D. Active-Damping-Based Field-Weakening Control Strategy with Voltage Angle Regulation for High-Speed SPMSM Drive. *IEEE Trans. Ind. Electron.* **2023**, *71*, 1421–1431. [CrossRef]
14. Wang, C. Novel Flux-Weakening Control of Permanent Magnet Synchronous Machines with Particular Reference to Stability Issues. Ph.D. Thesis, University of Sheffield, Sheffield, UK, 2019.
15. Bolognani, S.; Calligaro, S.; Petrella, R. Adaptive Flux-Weakening Controller for Interior Permanent Magnet Synchronous Motor Drives. *IEEE J. Emerg. Sel. Top. Power Electron.* **2014**, *2*, 236–248. [CrossRef]
16. Bozhko, S.; Rashed, M.; Hill, C.I.; Yeoh, S.S.; Yang, T. Flux-Weakening Control of Electric Starter–Generator Based on Permanent-Magnet Machine. *IEEE Trans. Transp. Electrific.* **2017**, *3*, 864–877. [CrossRef]
17. Zhang, Y.; Xu, L.; Güven, M.K.; Chi, S.; Illindala, M. Experimental Verification of Deep Field Weakening Operation of a 50-kW IPM Machine by Using Single Current Regulator. *IEEE Trans. Ind. Appl.* **2011**, *47*, 128–133. [CrossRef]

18. Lei, Z.; Xuhui, W.; Feng, Z.; Liang, K.; Baocang, Z. Deep Field-Weakening Control of PMSMs for Both Motion and Generation Operation. In Proceedings of the 2011 International Conference on Electrical Machines and Systems, Beijing, China, 20–23 August 2011; pp. 1–5. [CrossRef]
19. Stojan, D.; Drevensek, D.; Plantic, Z.; Grcar, B.; Stumberger, G. Novel Field-Weakening Control Scheme for Permanent-Magnet Synchronous Machines Based on Voltage Angle Control. *IEEE Trans. Ind. Appl.* **2012**, *48*, 2390–2401. [CrossRef]
20. Miyajima, T.; Fujimoto, H.; Fujitsuna, M. A Precise Model-Based Design of Voltage Phase Controller for IPMSM. *IEEE Trans. Power Electron.* **2013**, *28*, 5655–5664. [CrossRef]
21. Kwon, Y.-C.; Kim, S.; Sul, S.-K. Six-Step Operation of PMSM with Instantaneous Current Control. *IEEE Trans. Ind. Appl.* **2014**, *50*, 2614–2625. [CrossRef]
22. Kwon, T.-S.; Sul, S.-K. A Novel Flux Weakening Algorithm for Surface Mounted Permanent Magnet Synchronous Machines with Infinite Constant Power Speed Ratio. In Proceedings of the International Conference on Electrical Machines and Systems (ICEMS), Seoul, Republic of Korea, 8–11 October 2007; pp. 440–445. [CrossRef]
23. Liu, H.; Zhu, Z.Q.; Mohamed, E.; Fu, Y.; Qi, X. Flux-Weakening Control of Nonsalient Pole PMSM Having Large Winding Inductance, Accounting for Resistive Voltage Drop and Inverter Nonlinearities. *IEEE Trans. Power Electron.* **2012**, *27*, 942–952. [CrossRef]
24. El-Refaie, A.M.; Jahns, T.M. Optimal Flux Weakening in Surface PM Machines Using Fractional-Slot Concentrated Windings. *IEEE Trans. Ind. Appl.* **2005**, *41*, 790–800. [CrossRef]
25. El-Refaie, A.M.; Jahns, T.M.; McCleer, P.J.; McKeever, J.W. Experimental Verification of Optimal Flux Weakening in Surface PM Machines Using Concentrated Windings. *IEEE Trans. Ind. Appl.* **2006**, *42*, 443–452. [CrossRef]
26. Morimoto, S.; Sanada, M.; Takeda, Y. Effects and Compensation of Magnetic Saturation in Flux-Weakening Controlled Permanent Magnet Synchronous Motor Drives. *IEEE Trans. Ind. Appl.* **1994**, *30*, 1632–1639. [CrossRef]